

# KaRIn Alignment Mechanism Design, Development, and Testing

John Luke Wolff\*

## Abstract

The **Ka-Band Radar Interferometric System (KaRIn)** will characterize the ocean mesoscale/sub-mesoscale circulation and provide a global inventory of all lakes, reservoirs, wetlands, and major rivers. There are two identical Alignment Mechanisms (AM) mirrored on the instrument to correct KaRIn Azimuth radar pointing errors. Each AM is a one-degree-of-freedom precision mechanism. The mechanism must meet challenging thermoelastic distortion requirements over a wide temperature range. The flight design was qualified in less than two years, and the flight hardware is currently in acceptance testing. Discussed are key design details along with supporting development and qualification test results.

## Introduction

The KaRIn instrument uses radar interferometry to perform science measurements, which dictates tight alignments between the respective radar elements. The instrument requires a series of deployments, as shown in Figure 1. The AM enables the KaRIn instrument to correct residual post-deployment antenna pointing errors. The choice to maintain pointing passively imposed challenging thermoelastic distortion requirements on the AM. To simplify the mechanism overall complexity, launch locks are not used. Each AM consists of a Mechanism Strut Assembly (MSA) and Rotation Flexure Assembly, shown in Figure 2. The Rotation Flexure Assembly contains a hexfoil rotary flexure, which acts as the mechanism pivot axis for the one-degree-of-freedom commanded motion. The mechanism pivot axis is configured such that rotations about the pivot axis are linearly proportional to KaRIn Azimuth angle. The MSA consists of single-blade and coaxial double-blade flexures to create a kinematic five-bar linkage configuration, with the diagonal strut element containing a Linear Actuator Assembly (LAA). The LAA can lengthen or shorten via a geared stepper motor with an ACME leadscrew output. This linear length change in the diagonal strut causes a parallelogram effect in the MSA. The parallelogram effect results in primarily a rotation about the mechanism pivot axis. The small extraneous angular motion in the orthogonal axis is acceptable. The key design requirements are summarized in Table 1.

*Table 1: Summary of Key Design Requirements*

Mechanical Environments	0.0 kHz to 0.1kHz: Sine Input, Peak 38G, All 3-Axes 0.1 kHz to 2.0kHz: Random Input, 6.8 G <sub>rms</sub> , All 3-Axes Note: Structurally support additional mass (NTE 4.6kg)
Thermal Environments	Non-Operation: -95°C to +100°C Operation: -35°C to +100°C Note: Operation limit includes motor self-heating
Thermoelastic Distortions	Relative Azimuth: 2mdeg (1-sigma) Note: Based on on-orbit temperature predictions
Commanded Motion	Accuracy: <6% of commanded motion Resolution: 0.6 mdeg Range of Motion: 150 mdeg to 250 mdeg Note: Step rate chosen to be 10Hz based on electronics

---

\* Jet Propulsion Laboratory, California Institute of Technology, Pasadena, CA

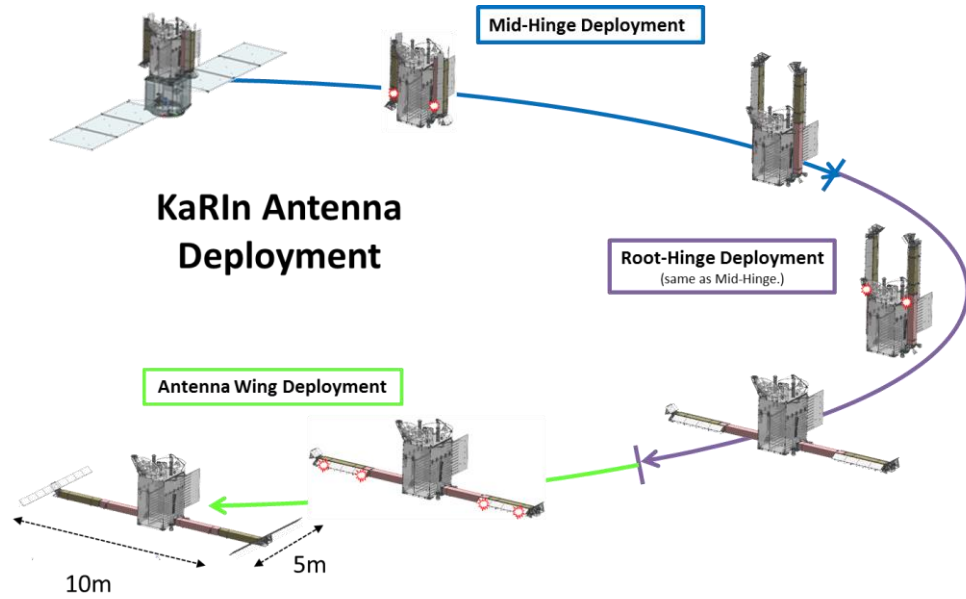


Figure 1: KaRIn Antenna Deployment

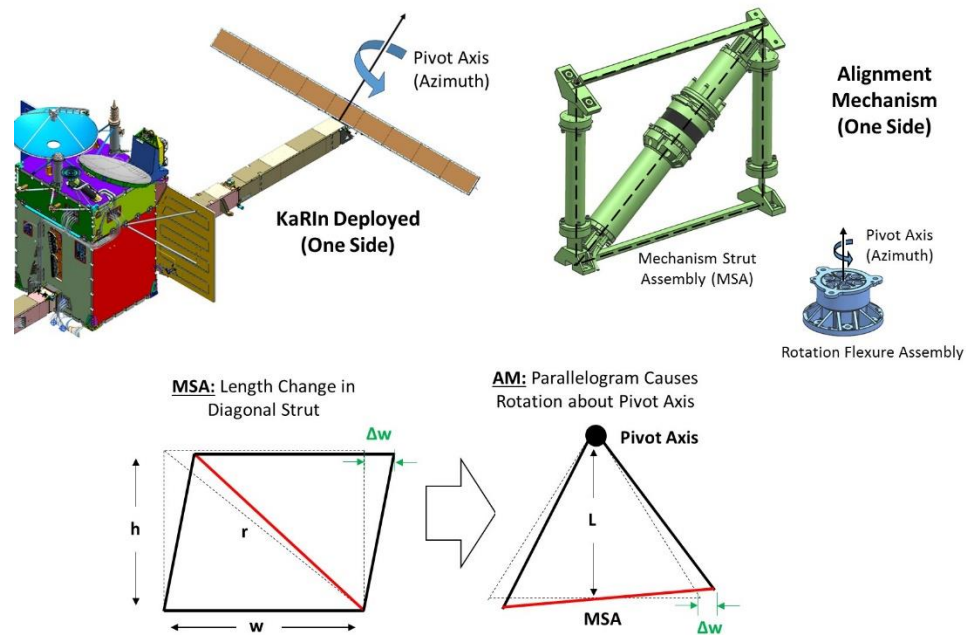


Figure 2: Alignment Mechanism Configuration

## Design Overview for Thermoelastic Distortions

KaRIn Azimuth thermoelastic distortions, caused by the MSA, are the primary concern due to the instrument's strong sensitivity to this parameter. Therefore, this paper focuses solely on those thermoelastic distortions. The MSA 1D-thermoelastic distortion model, see Eq. 1, has been validated by FEM (Finite Element Model) and by testing, which is discussed later in this paper. Eq. 2 is the uncertainty in the model. For each key term, the partials are shown in Figure 3. Summarized in Table 2 are the model uncertainties and associated mitigation approaches. The dominant error sources are the coefficient of thermal expansion (CTE) uncertainty<sup>1</sup> and 3D thermoelastic distortions due to bolt slip.

<sup>1</sup> Includes hysteresis between thermal cycles, measurement error, and unit-unit variability.

### Coefficient of Thermal Expansion (CTE)

To use reference sources ([1], [2]) for instantaneous CTE over temperature, the thermoelastic distortion model would need to incorporate unacceptably high CTE uncertainties. To mitigate this risk, all flight piece parts, except the LAA, were fabricated from controlled slabs of material whose CTE was characterized per ASTM E289<sup>2</sup>. To build confidence in the CTE over temperature for the LAA, a flight-like LAA was built, with the CTE measured per ASTM E289. Due to difficulties controlling all of the materials in the LAA, the team continued to assume a large CTE uncertainty for the LAA until the flight LAAs were each measured. In figure 5, the measured instantaneous CTE over temperature is compared to several reference sources. All CTE uncertainties used in the model are summarized in Table 3.

### Thermoelastic Distortion due to Bolt Slip

As the temperature is changed for CTE mismatched materials bolted together, radial strain increases until joint friction due to bolt preload is overcome, whereby radial strain projects into axial distortion errors. Where possible, this error source was eliminated by adding radial flexures to one side of the bolted joint to eliminate radial coupling at the bolted joint. At all other bolted joint locations, a low friction surface coating was applied to improve our confidence in the design and the repeatability. At these bolted joints, thermoelastic distortion uncertainty was empirically estimated by varying in the FEM the radial stiffness at each bolted joint location for a 10°C bulk soak case. Then, the FEM results were linearly scaled based on closed form solutions estimating the maximum temperature change required for each bolted joint to slip.

$$\delta\theta = 1/L \left[ (r/w)\delta r - (h/w)\delta h - \delta w \right] \quad (1)$$

$$\partial(\delta\theta) = 1/L \sqrt{[(r/w)(\partial\{\delta r\})]^2 + [(h/w)(\partial\{\delta h\})]^2 + [\partial\{\delta w\}]^2} \quad (2)$$

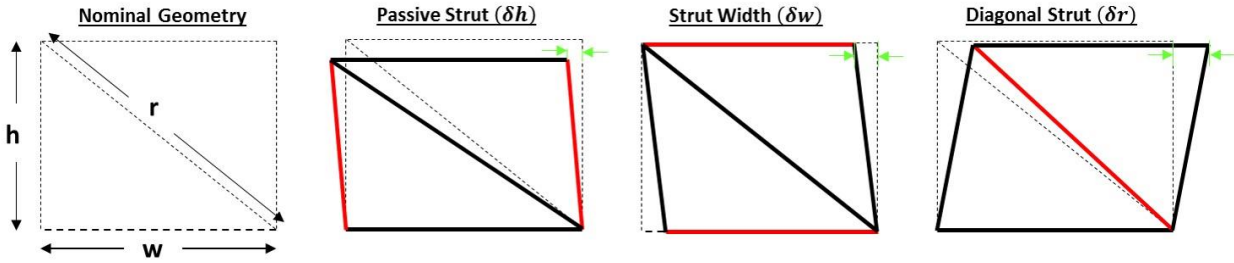


Figure 3: Mechanism Strut Assembly Thermoelastic Distortions Key Terms

Table 2: Thermoelastic Distortion Uncertainty Error Sources

Uncertainty Sources	Mitigation – Design Intent	Development Test (Prior to Mechanism Level Test)
Temperature (Gradient)	Top-to-bottom and left-to-right, materials chosen are nearly symmetric. Minimize CTE by utilizing High Purity (HP) Invar36 <sup>3</sup> where possible. See Figure 4.	None
Temperature (Bulk)		
Coefficient of Thermal Expansion	Metallic hardware and bolted joints to improve confidence in incorporating test results to model predicts.	Characterize CTE for flight material and prototype LAA. Final verification, characterize CTE for each flight LAA.
3D Effect (due to bolt slip)	Radial flexures where configuration allows OR low friction surface coating (SF-2).	None
Linear Lengths	Control fabrication/assembly tolerances.	Inspect part/assembly tolerances.

<sup>2</sup> Five coupons machined from each slab of material, with three thermal cycles measured per coupon.

<sup>3</sup> HP Invar36 exhibits very good dimensional stability properties. While not discussed further in this paper, HP Invar36 is critical to the mechanism temporal stability performance [4].

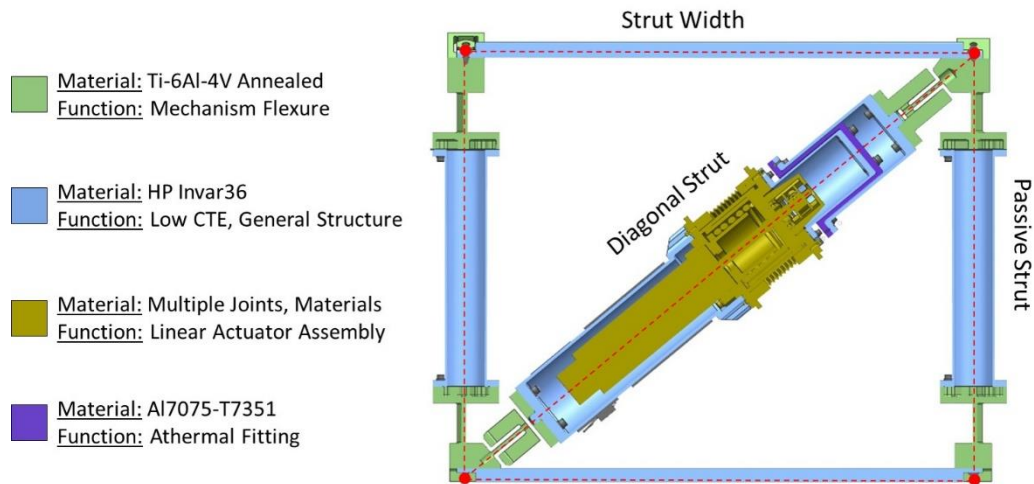


Figure 4: Mechanism Strut Assembly Configuration

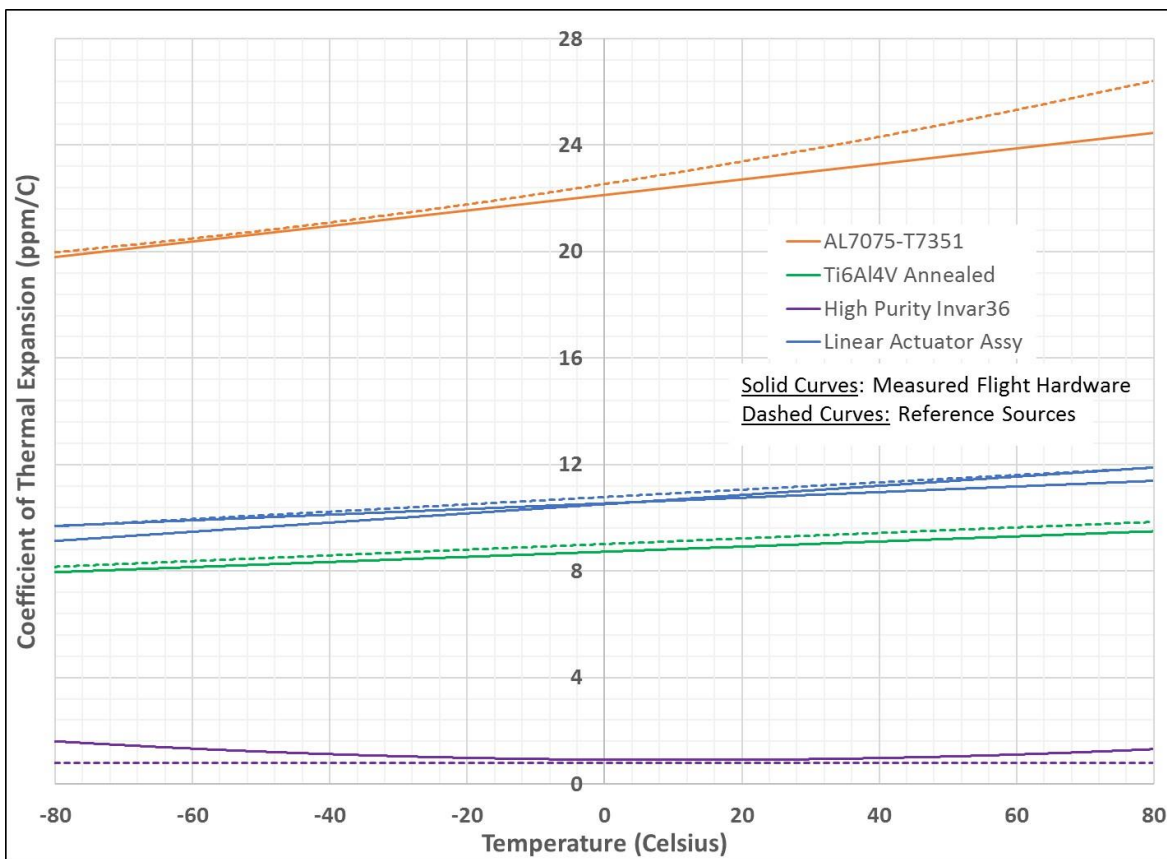


Figure 5: Instantaneous CTE over Temperature

Table 3: CTE Uncertainty

	Ti6Al4V Annealed	Al7075-T7351	HP Invar36	LAA 1	LAA 2
Reference Value (% of Mean CTE)	---	---	---	0.40 ppm/C (3.7%)	
Measured Flight (% of Mean CTE)	0.11 ppm/C (1.3%)	0.13 ppm/C (0.6%)	0.06 ppm/C (8.2%)	0.20 ppm/C (1.9%)	0.32 ppm/C (3.0%)

## Key Design Features

Illustrated in Figure 6 are the mechanism key design features. The bolt spacers increase the bolt length and thereby limit thermally induced bending stresses in the respective bolts. The single blade flexures, coaxial double blade flexures, and the rotation flexure provide the necessary boundary conditions to achieve a quasi-kinematic structure. KaRIn thermoelastic distortions are verified by analytically combining subsystem test data into the instrument level Structural Thermal Optical model. Therefore, it is critical to limit interface distortions, as they are not captured in the respective tests. The thermoelastic distortions due to the MSA interfaces are removed by the presence of the strut interface bar in conjunction with the respective radial flexures. The mechanism is nominally athermalized via an athermal fitting, illustrated in Figure 4. The remaining radial flexures remove thermoelastic distortion uncertainty.

### Flexure Design

All flexures were fabricated by electrical discharge machining (EDM), with the titanium flexures requiring chemical etching post-machining to remove the beta-alpha recast layer. Trade studies were completed to balance the competing design considerations, summarized in Table 4. To determine the appropriate FEM mesh density for stress analysis, it is recommended to have at least two nodes across the fillet region and the flexure thickness. To limit the FEM file size, the FEM mesh density was not sufficient to assess the radial flexures stresses. The radial flexure stresses were analyzed using beam shear, beam axial, and beam bending free body equations for the respective load cases, illustrated in Figure 7. The flexure fillet radii were selected to limit the stress concentration factor to 1.5 [3]. The flexure margins were analyzed at the worst-case manufacturing geometry tolerances. The bolt install torque is critical to include in the radial flexure stress margins. Where appropriate, flexure stress margins also need to include imposed deflections due to mechanism motion.

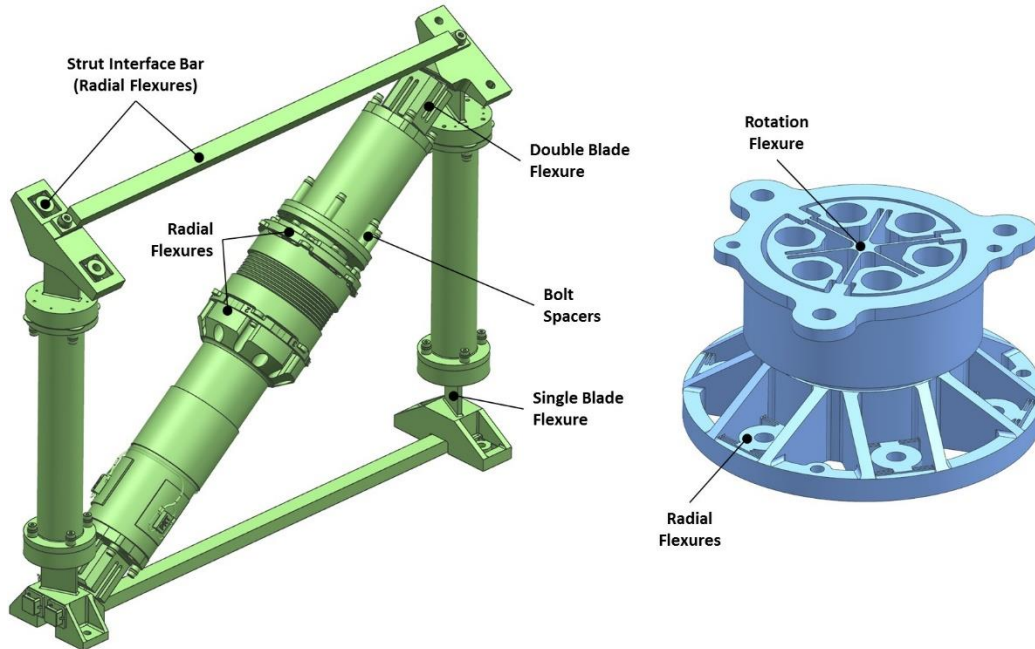


Figure 6: Key Design Features in Alignment Mechanism

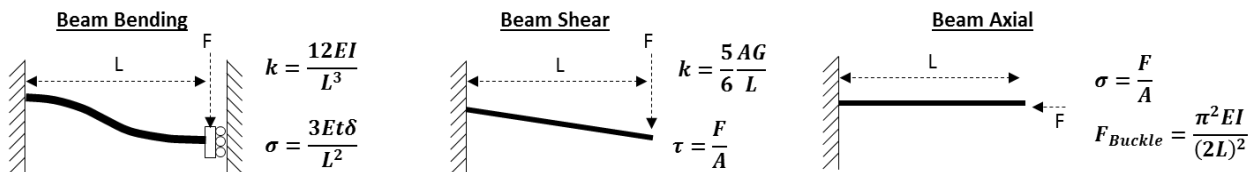


Figure 7: Radial Flexure Free Body Diagrams



Table 4: Flexure Design Considerations

Location	Flexure Function	Flexure Design Driver: Stiffness	Flexure Design Driver: Stress
Single Blade Flexure (Thick:2.00±0.05mm)	Kinematic B.C. (5-Bar Linkage)	1) <u>Bending</u> : LAA force required for mechanism motion 2) <u>Axial</u> : KaRIn Deployed 1 <sup>st</sup> mode	Mechanism range of motion
Double Blade Flexure (Thick:1.75±0.05mm)		1) <u>Bending</u> : Assembly 2) <u>Axial</u> : KaRIn Deployed 1 <sup>st</sup> mode	Mechanical environments (and diagonal strut mass)
Hexfoil Rotary Flexure (Thick:0.60±0.05mm)	Mechanism Pivot Axis	1) <u>Torsion</u> : LAA force required for mechanism motion 2) KaRIn Deployed 1 <sup>st</sup> mode	Mechanical environments (and supported mass)
Radial Flexures (Thick:0.30±0.05mm)	Thermoelastic Distortion	1) <u>Radial</u> : Thermoelastic model prediction accuracy/repeatability 2) <u>Axial</u> : KaRIn Deployed 1 <sup>st</sup> mode	1) Thermal environments 2) Mechanical environments with bolt install torque added

### Linear Actuator Assembly Design

Key LAA design features are illustrated in Figure 8. The LAA converts commanded rotational steps from the actuator into linear steps required by the mechanism. As the LAA is part of the primary load path, it must react large axial, lateral, and bending loads as well as contribute to the MSA thermoelastic distortion. To gain confidence in the design, a prototype LAA was built early in the design phase. The main objectives with the prototype LAA were to characterize the linear step size and the effective axial instantaneous CTE over temperature. Summarized in Figure 9 is the LAA test setup along with annotated test data graphs. The LAA key performance metrics are summarized in Table 5.

The actuator consists of a 3-phase stepper motor, 2-stage planetary gearhead, thrust module with a hard-shimmed leadscrew, and hall sensor assembly for confirming step integrity (not motor commutation). Except for the thrust module, the actuator consists of entirely flight heritage components, which allowed for a short procurement and development timeline. The thrust module relies on a pair of needle roller thrust bearings to improve the axial load capability and axial stiffness within a small packaging volume. As the LAA was only preloaded for mechanism operations, the actuator gaps in the axial direction during launch and vibration testing. The dynamic axial stiffness was estimated as being one-half the static axial stiffness.

The telescoping cylindrical plain bearing housings provided high bending stiffness during high bending load events, like launch or vibration testing. To estimate the bending stiffness, a non-linear contact FEM was required. The Inner Bearing Housing was greased plated C63200 (Aluminum-Bronze). The Outer Bearing Housing and the Leadscrew were fabricated from CRES 15-5PH condition H1025. The plain bearing housings had tight diameter tolerances and used a 1.0 length to diameter ratio, thereby ensuring minimal dynamic effects and minimal bending loads transferred through the actuator<sup>4</sup>. When assessing the concentricity of the bearing housings to the leadscrew, it is advantageous to include the ACME radial play.

Table 5: Linear Actuator Assembly (LAA) Key Characteristics

Characteristic	Value	Notes
Total Mass	270 grams	As built, includes harnessing
Interface Loads (Approximate)	Axial: 1,800 N Shear: 700 N Moment: 400 N*m	Quasi-static equivalent. Dynamic analysis used to verify margins and make test predicts.
Dynamic Stiffness (Approximate)	Axial: 32,000 N/mm Moment: 14,000 N*m/rad	Torsional stiffness is high due to bellows.
Range of Motion	600 µm to 1,000 µm	As built shown. Mechanism capable of 2,160+ µm.
Nominal Step Size	(0.5) µm ± 6%	Characterize mechanism step size over ROM

<sup>4</sup> Leadscrew has a reduced diameter between ACME thread interface and actuator, thereby further limiting the lateral and bending loads transferred through the actuator.

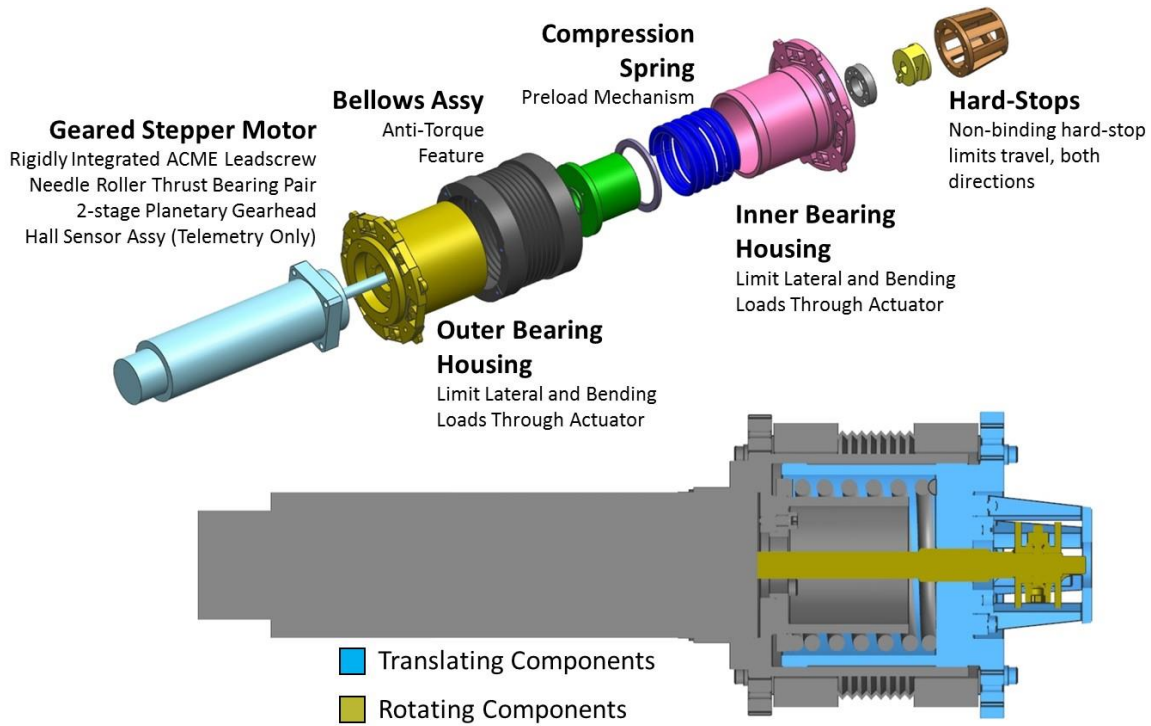


Figure 8: Linear Actuator Assembly Key Design Features

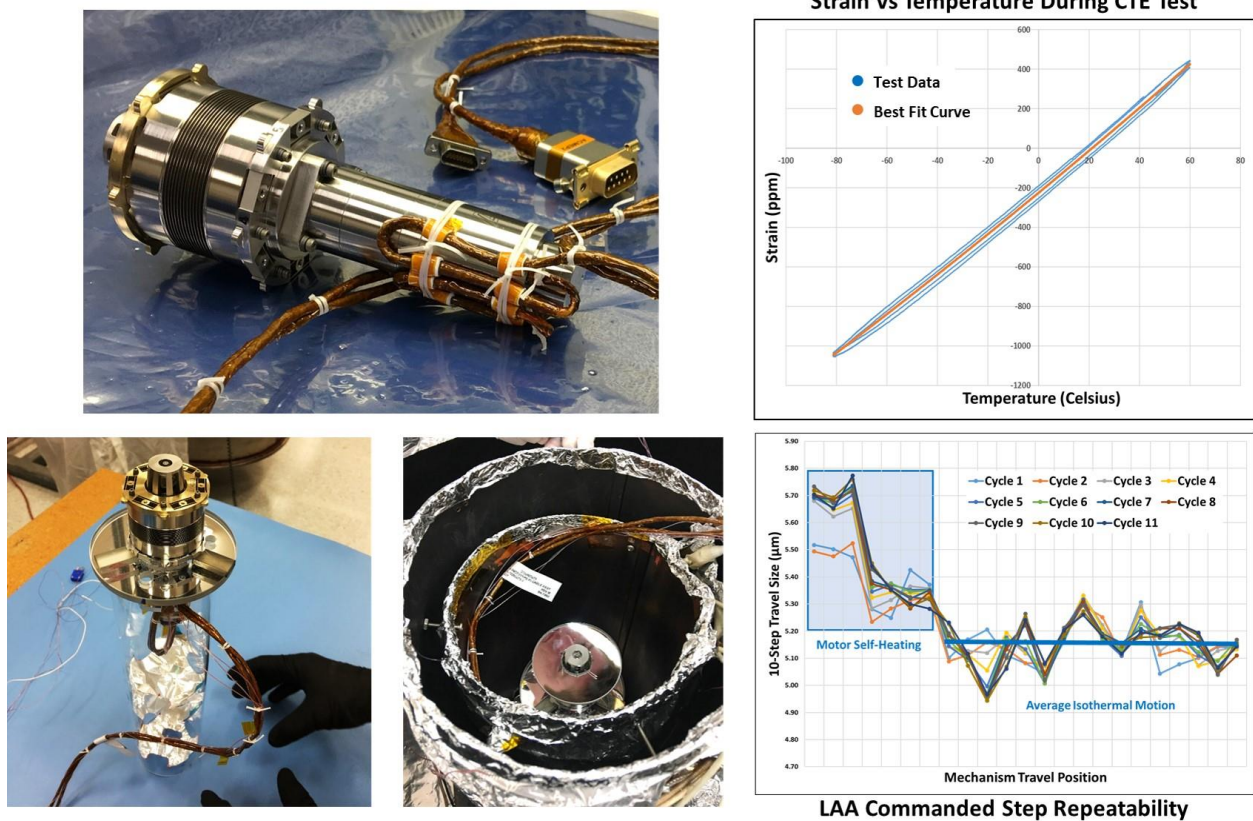


Figure 9: Prototype Linear Actuator Assembly Testing (Setup and Key Test Data Graphs)

## Commanded Motion Functional Testing

Before and after vibration testing, an auto-collimator coarsely measured the mechanism motion, where the objective was to verify mechanism step repeatability. The hall sensors provide feedback on the motor step integrity. While the mechanism is integrated with the vibration GSE hardware, a mirror is attached near the top of the rotation flexure. See Figure 10, the mechanism motion was repeatable in both directions, and the hall sensors measured no missed or skipped motor steps. A nearly perfect quadratic best-fit curve matches both sets of data to better than 2%, which is better than expected when considering the crude test setup. When the mechanism changes stepping direction or runs into either mechanical hard stop, there will be a dead band zone. The test setup illustrated in Figure 15 will be used to create the calibration curves at temperature limits for the mechanism motion, as well as measure the dead band zones and extraneous motion about other axes; this test is planned for late January 2018.

By substituting Equation 3 into Equation 1, where  $\delta h$  and  $\delta w$  equal zero, the mechanism motion could be estimated. However, this produced an over-estimate when compared to the motion actually measured, with the difference being roughly 20%. Some variance due to the ACME lead, flexure geometry, or mechanism geometry is expected, but not to this magnitude. The auto-collimator appeared clocked at a  $20^\circ$ , which would cause a trigonometric projection error. Since we were borrowing the auto-collimator from another team, the author did not tinker with their hardware. In addition, thermoelastic distortions due to motor self-heating would cause a similar effect seen in Figure 10. During LAA commanded step repeatability testing, summarized in Figure 9, a quasi-isothermal environment was achieved, whereas this functional test did not. While not important for this functional test, this oddity merits some further investigation if it is observed during later characterization testing of the mechanism isothermal motion.

$$\delta r = n \frac{\gamma N}{2\pi} \quad (3)$$

N: Commanded Steps,  $\gamma$ : Geared Motor Output Angle (rad), n: ACME Lead

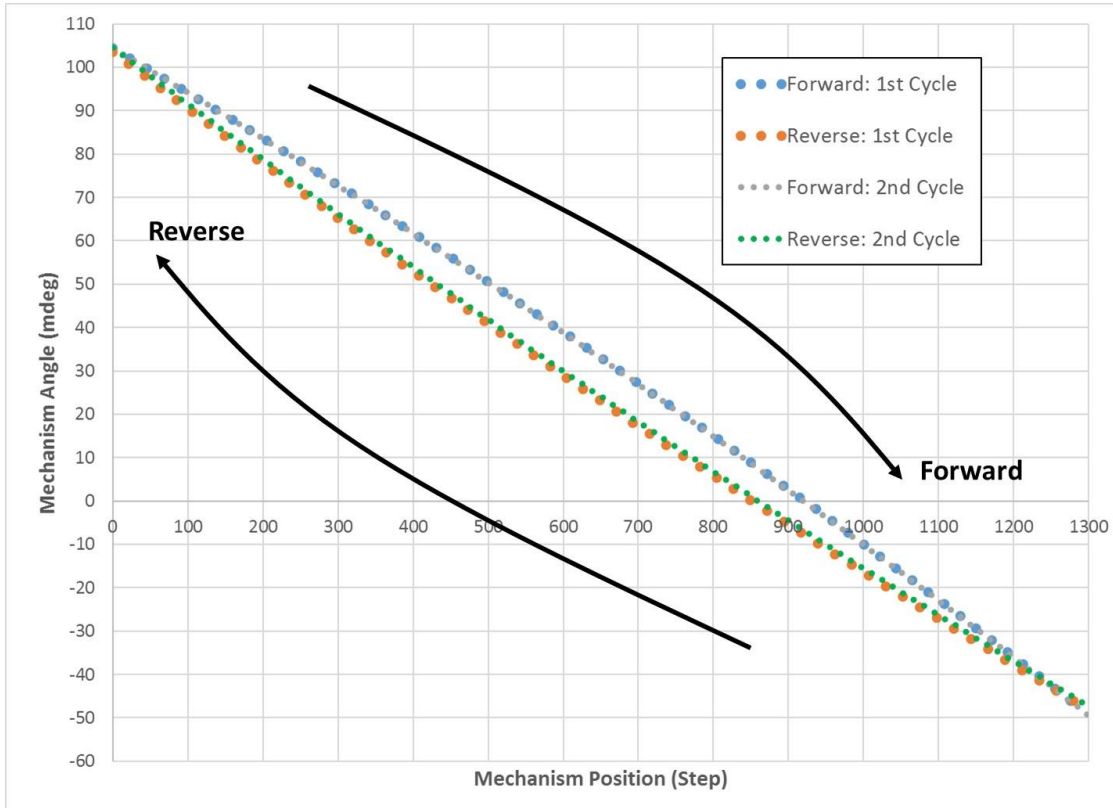


Figure 10: Mechanism Functional Test (Pre & Post Vibration Testing)



## Vibration Testing

Figure 11 illustrates the test configuration and the test instrumentation, with the environments previously summarized in Table 1. The diagonal strut first bending mode (Y-Axis Input, Sine) and the first global mode of the mechanism (X-Axis Input, Random) drive the mechanism design minimum stress margins. The four single axis accelerometers mounted on the LAA in 45° increments measure the responses of the diagonal strut first bending mode. The force transducers at the base of the mechanism measure the mechanism global mode responses and they are used to force limit during random vibration testing.

The mass simulator was designed to be a rigid body, which simulates the mass properties of hardware mounted to the AM in the flight configuration during launch. All test predicts used a coarse mesh density for the mass simulator FEM. As mechanical environments evolve late in the project, the coarse mesh density allowed the team to complete the dynamic pre-test analysis in a timelier manner. Table 6 illustrates the modal mass comparison between the two FEMs. In general, the mode frequencies are higher with the finer meshed GSE FEM, supported by the test results in Figure 12. As input decreases at higher frequencies, typically higher stiffness results in lower stresses. For Random-X, force (RMS) was measured 15% higher than predicts, which is acceptable based on the stress margins of safety.

As previously discussed, the LAA initially transfers small bending loads through the leadscrew and then, as the loads are further increased, transitions to the cylindrical bearing housings being the primary bending load path. For X-axis and Y-axis inputs, the transition from soft to stiff bending load path appears clearly in the single-axis accelerometer responses around 45Hz, see Figure 13. Above 80Hz, the response appears to deviate from the predicts for the Y-Axis Sine input, which seems at least partially due to the input not ramping down entirely. Figure 14 shows the diagonal strut first bending mode frequency came close to predicts. Interestingly, the diagonal strut first rigid bending mode does not appear for the Z-axis input, which is likely due to the input levels being insufficient to engage the cylindrical bearing housing load path.

The AM vibration test envelopes the stresses within the AM flight hardware during all higher level of assembly vibration testing. During vibration testing, the hall sensors monitored the motor rotor position, which verified the motor did not back-drive. While the mechanism does still move during vibration testing due to ACME thread resettling and 0.2% plastic deformation, the motion is small relative to the mechanism range of motion (ROM). Random vibration signature runs pre- and post- 0dB level test runs verify no change greater than 5%. As a mechanism functional health check, the mechanism stepped through its ROM after each test axis, with the hall sensor data used to verify the step integrity. After all vibration testing, an auto-collimator measures the mechanism stepping through its ROM, with the results previously discussed.

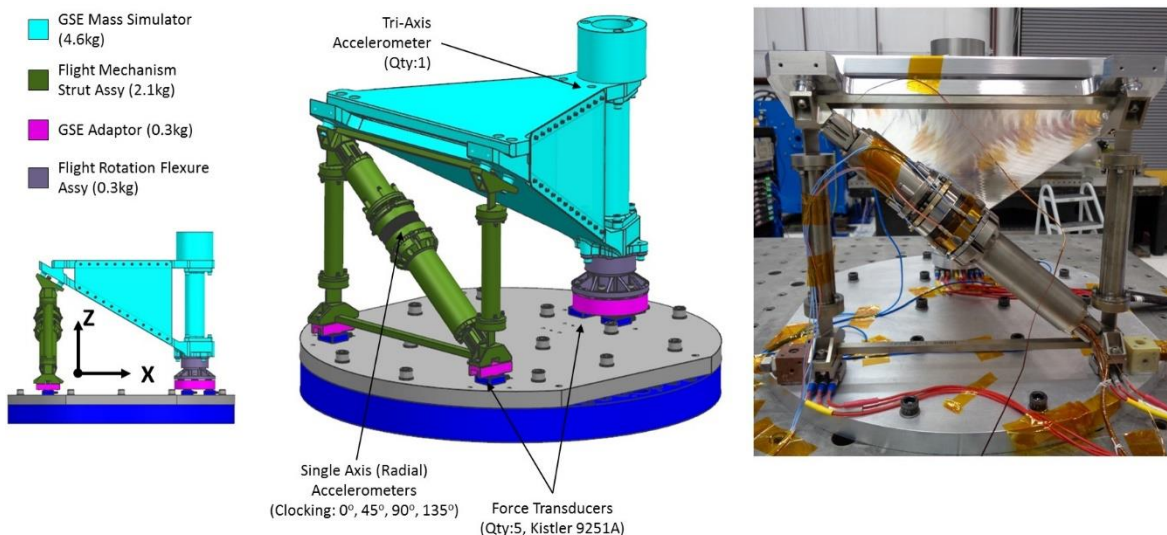


Figure 11: Alignment Mechanism Vibration Test Configuration

Table 6: GSE FEM Mesh Density Modal Comparison

(a) Coarse Mesh, GSE FEM					(b) Fine Mesh, GSE FEM				
Mode	Frequency	X-Input	Y-Input	Z-Input	Mode	Frequency	X-Input	Y-Input	Z-Input
2	111 Hz	0%	14%	10%	2	115 Hz	0%	16%	10%
3	119 Hz	29%	0%	0%	3	123 Hz	25%	0%	0%
4	183 Hz	11%	51%	1%	4	181 Hz	1%	59%	1%
5	191 Hz	44%	12%	0%	5	213 Hz	49%	3%	1%
9	321 Hz	1%	0%	47%	9	354 Hz	1%	0%	0%
10	360 Hz	1%	0%	1%	10	422 Hz	3%	0%	60%

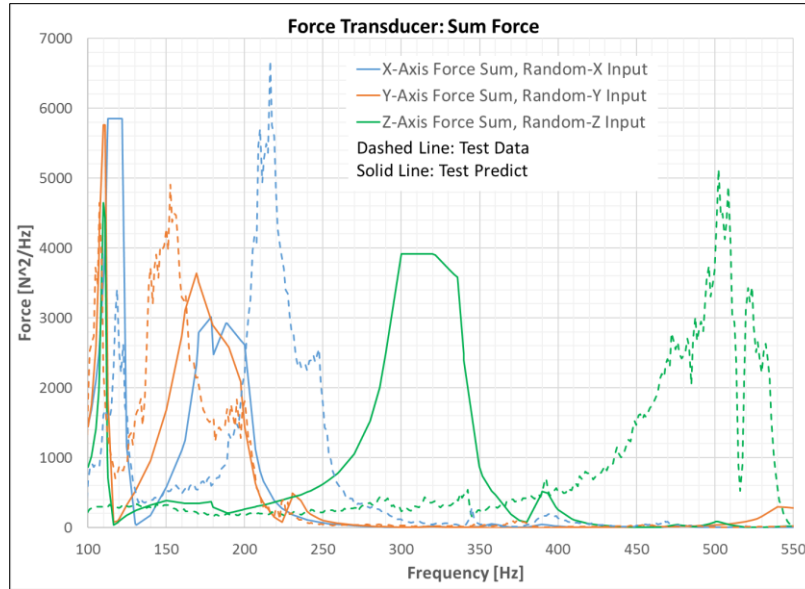


Figure 12: Random Vibration Test, Mechanism 1st Global Mode <sup>5</sup>

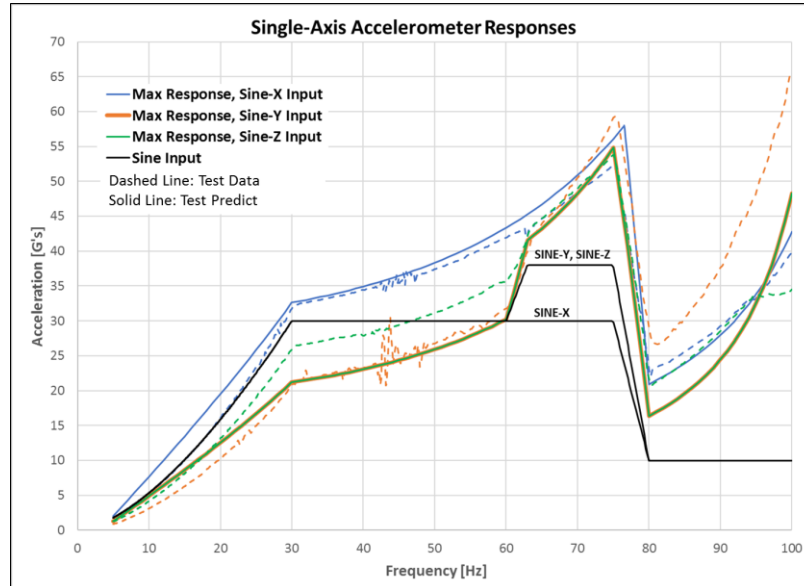


Figure 13: Sine Vibration Test, Single-Axis Accelerometer Responses

<sup>5</sup> To identify mode frequency, responses are normalized by force-limited inputs. When normalized, X/Y results align well with predicts. Z result is higher than predict, likely due to GSE mesh density too small.

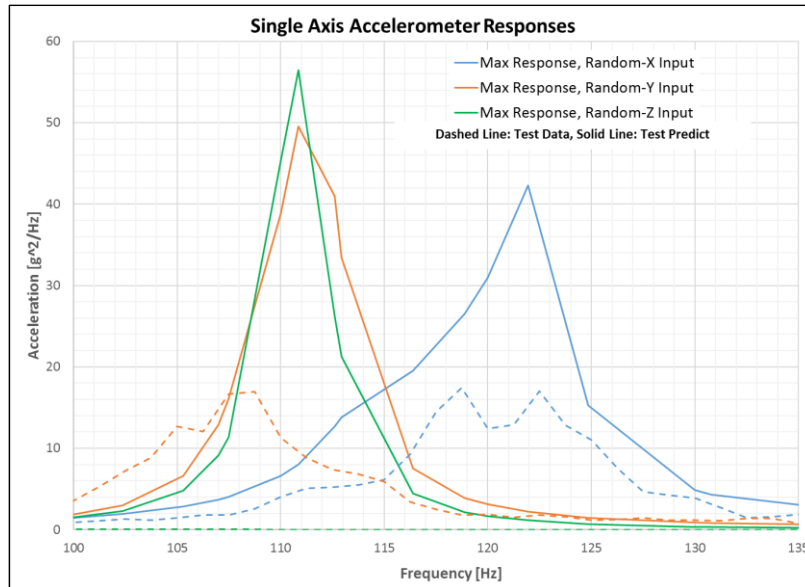


Figure 14: Random Vibration Test, Diagonal Strut 1st Bending Mode

### Thermoelastic Distortion Testing

Figure 15 illustrates the test configuration, which is done at Precision Measurement and Instrumentation Corp (PMIC). The test setup measures accurately the flight mechanism angular thermoelastic distortions about the mechanism pivot axis. When gradients are kept small (less than 5°C), the GSE is designed to not contribute to the thermoelastic distortion of concern. The 32-thermocouple-sensors are calibrated together with 4-silicone-diode-sensors (Lakeshore DT-670-SD-70H) providing reference absolute temperature measurements, with an accuracy better than 50mK. A PMIC proprietary setup measures the optical length between the laser and the detector. The base plate mounted mirror measures the bulk bias of the test setup. The mirror mounted near the top of the rotation flexure is the primary data point, with the mirrors mounted near the MSA intended as redundant measurements. The reduced chamber pressure is backfilled with helium to balance thermal conduction with optical measurement needs. Quartz rods support the test hardware with a quasi-kinematic interface. The quartz rods are mounted to a water-cooled plate.

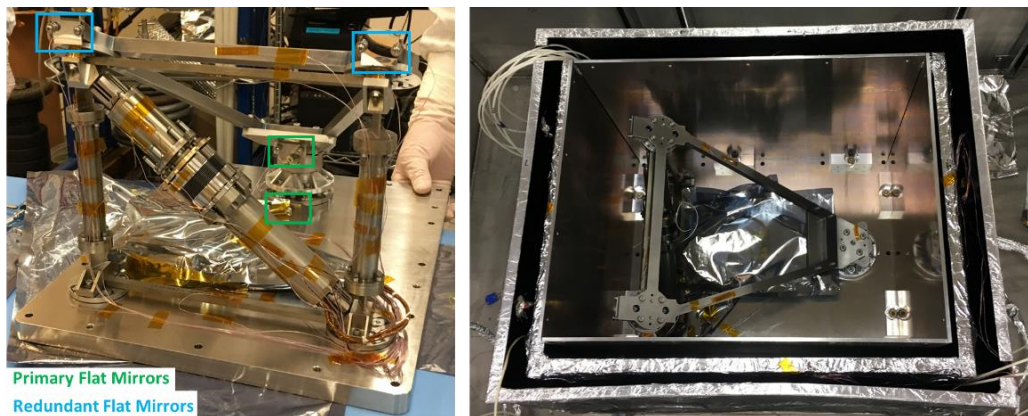


Figure 15: Thermoelastic Distortion Test Configuration

The GSE interfacing directly with flight hardware was titanium, which is the flight configuration, to ensure the radial flexures are not overstressed. The large GSE pieces on top and bottom are both Invar36 to minimize overall thermoelastic distortions. To eliminate thermoelastic distortion uncertainty between CTE-mismatched GSE hardware bolted together, radial flexures are implemented (26 flexures in the GSE). There are 24 temperature sensors mounted on the JPL hardware, where each segment illustrated in

Figure 16 has temperature directly measured during the test<sup>6</sup>. To predict the thermoelastic distortion based on measured temperatures, substitute Eq. 4-6 into Eq. 1. To estimate the prediction uncertainty, substitute Eq. 7-9 into Eq. 2, where length uncertainty ( $\partial L$ ) and temperature uncertainty ( $\partial T$ ) is negligible.

$$\delta r(T_i) = \sum_{i=1}^7 \{[\alpha_i][L_i][\Delta T_i]\} + \sum_{i=1}^4 \Delta x_i \quad (4)$$

$$\delta h(T_i) = \sum_{i=8}^{13} \{[\alpha_i][L_i][\Delta T_i]\} + \sum_{i=5}^6 \Delta x_i \quad (5)$$

$$\delta w(T_i) = \sum_{i=14}^{15} \{[\alpha_i][L_i][\Delta T_i]\} \quad (6)$$

$$\partial[\delta r] = \sqrt{\sum_{i=1}^7 \{[\partial \alpha_i][L_i][\Delta T_i]\}^2 + \sum_{i=1}^4 [\partial \Delta x_i]^2} \quad (7)$$

$$\partial[\delta h] = \sqrt{\sum_{i=8}^{13} \{[\partial \alpha_i][L_i][\Delta T_i]\}^2 + \sum_{i=5}^6 [\partial \Delta x_i]^2} \quad (8)$$

$$\partial[\delta w] = \sqrt{\sum_{i=14}^{15} \{[\partial \alpha_i][L_i][\Delta T_i]\}^2} \quad (9)$$

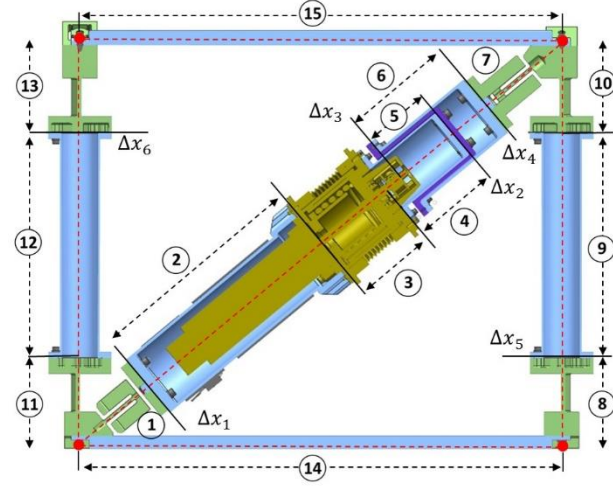


Figure 16: MSA Thermoelastic Distortion Variables

#### Test Anomaly: MSA Mirror Locations

Shortly after beginning the test, the two detectors pointed at the mirrors mounted near the MSA started measuring unexplained and unrepeatable angles. In addition, there was a large settling in the mirror mounted near the upper right in Figure 15 (passive strut only side), which became apparent when the test returned to room temperature. While the test only needs the two mirrors illustrated in Figure 15, the team is still investigating the anomaly with the two other locations. The team believes the prime culprit has to do with the instrumentation outside the chamber. To summarize what is going on, it is important to understand the laser measurements. The laser goes through beam steering optics and a single beam splitter optic before entering the chamber. The laser, detector, and optical levers are all mounted on different locations of the optical bench outside the chamber. However, the MSA mirror instrumentation is mostly grouped together, whereas the rotation flexure and base-plate mirror instrumentation are mostly grouped in another location. The team believes that the MSA mirror instrumentation is not properly attached to the respective mounts. However, to avoid disrupting the test, the investigation is on-hold until after the first mechanism completes the thermoelastic distortion testing in early January 2018. Therefore, only the two primary flat mirror locations illustrated in Figure 15 are discussed in this paper.

#### Test Results

While the test data processing is still on going for the first (of two) flight AM, the thermoelastic distortion model represented by Equation 1 appears to be validated by the test results. In Figure 17 and 18, the first cycle cooling-down from -40°C to -80°C is illustrated. The sample rate of the angular and temperature measurements was 0.2Hz. Per the pre-test calibration of the angular measurement, the angular measurement accuracy is better than 0.1 mdeg. In addition, there is roughly 0.25mdeg noise in the angular measurement. PMIC takes extreme measures to minimize noise in the system, but a crude low pass filter is still required. While a more extensive analysis could identify the correct frequency(s), a 12-point (1-minute) moving average best-fit curve seems appropriate to this author. The temperature measurement during the test is very stable. Based on thermocouple and silicon-diode calibration data, the temperature accuracy is better than  $\pm 0.2^\circ\text{C}$ . At thermal steady state, the temperature measurements align to within about  $0.5^\circ\text{C}$ , see Figure 18<sup>7</sup>. Summarized in Table 7, the last 12-point (1-minute) test data average is compared to the predictions, with the measured data being within the 1-sigma prediction envelope.

<sup>6</sup> The LAA bulk temperature was calculated as a linear average of several temperature measurements.

<sup>7</sup> Although thermocouples are uniquely calibrated/serialized, PMIC only uses standard curve to simplify implementation; PMIC controls shroud temperatures. In Figure 18, author incorporates calibration data.



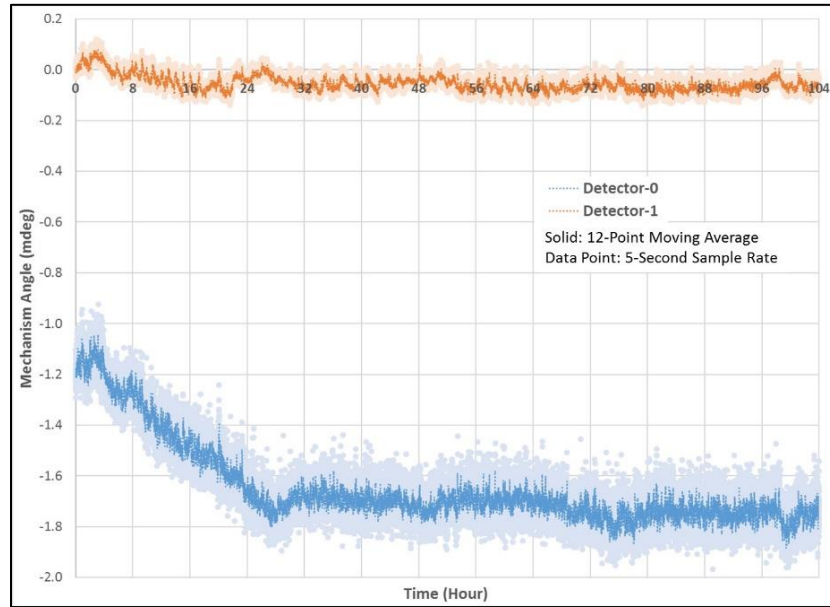


Figure 17: MSA Thermoelastic Distortion Angular Measurement

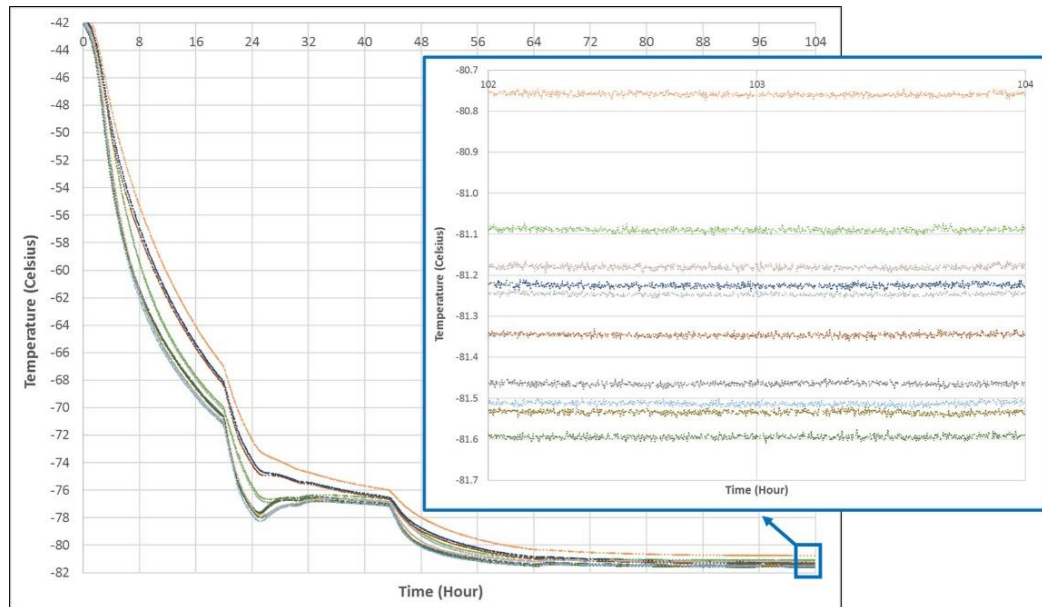


Figure 18: MSA Temperature Measurements

Table 7: MSA Thermoelastic Distortion Test Data Summary<sup>8</sup>

Approximate Bulk Temperature	Warming-Up		Cooling-Down	
	Data (mdeg)	Predict (mdeg)	Data (mdeg)	Predict (mdeg)
+80 Celsius	-0.70	$-0.95 \pm 0.45$	-1.16	$-1.02 \pm 0.45$
+20 Celsius	-0.20	$+0.00 \pm 0.35$	-0.10	$-0.05 \pm 0.35$
-40 Celsius	+0.90	$+0.49 \pm 0.45$	+0.88	$+0.46 \pm 0.45$
-80 Celsius	+1.11	$+1.22 \pm 0.50$	+1.39	$+1.12 \pm 0.50$

<sup>8</sup> Initial measurement bias was subtracted from test data results summarized in Table 7.



## Lessons Learned

The Nedox SF-2 low friction coating caused significant issues. Some of the issues encountered include: lost all part serialization, baked out to wrong temperature (per industry/vendor specifications), and rough handling (deep marks visible in titanium). While process inspection and/or quality control points help prevent issues, post-machining activities can fall through the cracks due to their perceived low technical or programmatic risk. Therefore, it is important to consider a parts complexity (e.g. lead-time, cost) when deciding on the proper oversight at a vendor facility. The design team should carefully consider whether each post-machining activity is required, especially when requiring a third party vendor. If the activity is still required, the design team should strive to minimize masking and carefully manage the activity.

To limit the tunnel vision syndrome, this author actively engaged a broad set of senior personnel for constructive criticism of the design throughout the design cycle (not just at design reviews). While providing the obvious benefit of pointing out design shortcoming(s) along with potential solutions(s), they can also help provide cover from the continual battle of micromanagement by “others”. Ultimately, final design decision should always remain with the mechanism team, but the team should make design decisions with eyes open to the associated compromises. This was a large contributor to the team’s success.

## Conclusion

The mechanism has demonstrated by test the capability to survive the mechanical and thermal environments specified. Based on both FEM and test validation, the mechanism thermoelastic distortion has inherent hysteresis and uncertainty, but the characteristic over temperature is enveloped by a few simple 1-D equations. While the commanded motion has been demonstrated by test to be repeatable to better than the 6% requirement over the entire range of motion, the mechanism might not have a linear relationship between step size and angular motion. To achieve the thermoelastic distortion stability and the commanded motion performance required, understanding sub-micron motion is required, which drives the test setup requirements. While having limited resources (personnel, schedule, money), two high performance space mechanisms can be delivered in a short period (roughly two years).

### Key Future Work

- After the mechanism life cycle test program is complete, the mechanism will be disassembled. Of particular interest, the gapping/sliding surfaces will be inspected for unacceptable damage or wear.
- Commanded motion performance testing measuring isothermal mechanism motion, using identical setup discussed for thermoelastic distortion testing. Development tests have been completed:
  - Flight AM: functional test with auto-collimator, coarsely characterize angular motion at RT.

### Acknowledgements:

Mike Johnson, Don Sevilla, Kim Aaron, Gary Wang, Andy Kissil, and Kerry Klein for being a constant source of independent and constructive feedback from the concept design through flight hardware testing. The entire mechanism team: Brandon Metz (Electronics), ATA structural analysis support, Eddie Ketsiri (Drawing), Robert Demerjian (Manufacturing), Don Lewis (Materials). Last but not least, PMIC staff for working long shifts through the holidays! The research was carried out at the Jet Propulsion Laboratory, California Institute of Technology, under a contract with the National Aeronautics and Space Administration

## References

1. MIL-HDBK-5J-1. (2003). *Metallic Materials and Elements for Aerospace Vehicle Structures*. Department of Defense.
2. Touloukian, Y., Kirby, R., Taylor, R., & Desai, P. (1975). *Thermal Expansion: Metallic Elements and Alloys (Volume 12)*. New York: Purdue Research Foundation.
3. Walter D. Pilkey, D. F. (2008). *Peterson's Stress Concentration Factors*. John Wiley & Sons.
4. Witold M. Sokolowski, S. F. (1993). Dimensional Stability of High-Purity Invar 36. *International Symposium on Optics, Imaging, and Instrumentation*. San Diego.